

# Ground-based remote sensing of aerosol properties using high resolution infrared emission and Lidar observations in the high Arctic

Denghui Ji<sup>1</sup>, Mathias Palm<sup>1</sup>, Christoph Ritter<sup>2</sup>, Philipp Richter<sup>1</sup>, Xiaoyu Sun<sup>1</sup>, Matthias Buschmann<sup>1</sup>, and Justus Notholt<sup>1</sup>

<sup>1</sup>Institute of Environmental Physics, University of Bremen, Otto-Hahn-Allee 1, 28359 Bremen, Germany

<sup>2</sup>Alfred Wegener Institute, Helmholtz Centre for Polar and Marine Research, Telegrafenberg A43, 14473 Potsdam, Germany

**Correspondence:** Denghui Ji (denghui\_ji@iup.physik.uni-bremen.de)

**Abstract.** Arctic amplification, the phenomenon that the Arctic is warming faster than the global mean, is still not fully understood. The Transregional Collaborative Research Centre TR 172 – Arctic Amplification: Climate Relevant Atmospheric and Surface Processes (AC)<sup>3</sup> funded by the DFG (German research foundation) contributes towards this research topic. For the purpose of measuring aerosol components, a Fourier-Transform Infrared Spectrometer (FTS) for measuring down-welling emission since 2019 and a Raman-Lidar are operated at the AWIPEV research base in Ny-Ålesund, Spitsbergen (79 °N, 12 °E). To do aerosol retrieval using measurements from the FTS, a retrieval algorithm based on the Line-by-Line Radiative Transfer Model and DIScrete Ordinate Radiative Transfer model (LBLDIS), is modified for different aerosol types (dust, sea salt, black carbon, and sulfate), aerosol optical depth (AOD) and effective radius ( $R_{\text{eff}}$ ). Using Lidar measurement, an aerosol and cloud classification method is developed for providing basic information about the distribution of aerosols or clouds in the atmosphere and used as an indicator to perform aerosol or cloud retrievals using the FTS. Therefore, a two-instruments joint observation scheme is designed and is performing on the data measured from 2019 to present. In order to show this measurement technique in details, a case study for an aerosol-only case is presented with data from the 10<sup>th</sup> of June 2020. In the aerosol-only case, the retrieval results show that sulfate ( $\tau_{900\text{cm}^{-1}}=0.007 \pm 0.0027$ ) is the dominant aerosol during the whole day, followed by dust ( $\tau_{900\text{cm}^{-1}}=0.0039 \pm 0.0029$ ) and black carbon ( $\tau_{900\text{cm}^{-1}}=0.0017 \pm 0.0007$ ). Sea salt ( $\tau_{900\text{cm}^{-1}}=0.0012 \pm 0.0002$ ), which has the weakest emission ability in the infrared waveband, shows the lowest AOD value. Such proportions of sulfate, dust and BC also show good agreement with MERRA-2 reanalysis data. Additionally, the comparison with a sun-photometer (AERONET) shows the daily variation of aerosol AOD retrieved from FTS to be similar with that of the sun-photometer. Using this method, long time period observations from April to August in 2020 are retrieved and presented. Sulfate is often present in the Arctic. It is higher in Spring and lower in Summer. Similarly, BC is also frequently observed in the Arctic, with less obvious seasonal variations than sulfate. A BC outburst event is observed in each Spring and Summer. In spring, sulfate and BC are dominant while sea salt and dust are relatively low. In addition, a sea salt enhancement event is observed in Summer time, which might be due to the melting of sea ice and emitted from nearby open water. From the retrieved results in long time period, none of them show a clear correlation, so they can be retrieved independent of each other.

## 1 Introduction

25 In the Arctic, near surface temperatures are rising much faster than those of the global mean (Wendisch et al., 2017). This phenomenon is called Arctic Amplification (Serreze and Barry, 2011; Wendisch et al., 2017; Previdi et al., 2021). In order to understand the causes and effects of the rapid warming in the Arctic, many studies focus on key processes contributing to Arctic amplification, like temperature feedback (Bony et al., 2006; Soden and Held, 2006), surface albedo feedback (Graversen et al., 2014) and cloud and water vapor feedback (Taylor et al., 2013; Philipp et al., 2020). The collaborative research program  
30 TR 172 (AC)<sup>3</sup> focuses on the Arctic Amplification<sup>1</sup>.

Apart from the physical feedback processes, aerosol has a large impact on the Arctic environment (Abbate et al., 2019; Schmale et al., 2021). Aerosol influences the Arctic climate by aerosol-cloud interactions (Fan et al., 2016) and aerosol-surface interactions (Donth et al., 2020). For example, Black Carbon (BC) deposits on snow and ice, lowering the surface albedo (Ming et al., 2009; Bond et al., 2013) and thus warming the surface. Dust, when present in layers over high albedo surfaces  
35 and/or deposited to the snow, will warm the atmosphere (Krinner et al., 2006); Sulfate, organic matter and sea salt may cool the Arctic by scattering light back to space and by modifying the microphysics of liquid clouds (Schmeisser et al., 2018). At cirrus temperatures, dust, ammonium sulfate and sea salt increase the cloud albedo by increasing ice crystal concentrations (Wagner et al., 2018).

In recent decades, mainly in-situ measurements of aerosols were performed in the Arctic. Most reports show that the aerosol  
40 composition is changing. Koch et al. (2011) and Ren et al. (2020) find that sulfate and BC are decreasing compared to the last century. Several projects in (AC)<sup>3</sup> also focus on BC concentration measurements (Kodros et al., 2018; Zanatta et al., 2018) and reveal the annual cycle of BC in the Arctic, higher in spring and lower in early summer (Schulz et al., 2019). Shaw (1995), Francis et al. (2018), Francis et al. (2019) find that dust can be transported over long distances into the Arctic and plays an important role in Arctic haze. In recent years, the area of open water has become larger, and the sea surface temperature is  
45 increasing, which leads to a local increase of the emission of sea salt (Domine et al., 2004; Struthers et al., 2011; May et al., 2016). Thus, during the Arctic warming period, the proportions of different aerosols in the Arctic also change.

There are several ways to measure the aerosol composition, such as remote sensing from satellite or ground-based instruments, in-situ measurement on the surface or from aircraft. Satellite instruments can provide measurements of large areas but are not very suitable in the Arctic due to the frequent existence of clouds and snow/ice on the surface, which make the measurements challenging (Lee et al., 2021). The in-situ measurements provide much more accurate measurements, but are often  
50 limited to the planetary boundary layer, have limited coverage and are sparse in time. Ground-based remote sensing provides measurements with a similar measurement geometry than satellites which are not confined to a particular altitude, unlike in-situ measurements. They provide time series measurements from the surface and has a similar viewing geometry as the satellite. Hence, a combination of different measurement methods is necessary to provide a complete picture of aerosols in the Arctic.  
55 In this paper, we focus on a passive ground-based remote sensing method in the thermal infrared to retrieve the aerosol components. Using atmospheric thermal emission spectra, measured by a Fourier Transform spectrometer (FTS), we perform a

---

<sup>1</sup>[www.ac3-tr.de](http://www.ac3-tr.de)

retrieval of aerosol properties as proposed by Rathke et al. (2002). Turner (2008) extended this method to dust measurements. Previous studies (Rathke et al., 2002; Turner, 2008) are limited to a specific type of aerosol, such as sulfate or dust. Based on them, this paper will further expand the number of aerosol types that can be measured by FTS.

60 In section 2, the location of measurement site and the setup of two instruments are described. Section 3 presents the joint observation scheme using two instruments (Lidar KARL and the Fourier Transform spectrometer, NYAEM-FTS) and information of the retrieval algorithm for NYAEM-FTS, including details of look-up tables of aerosol scattering properties. Section 4 shows the results of both KARL and NYAEM-FTS measurements in one case study of an aerosol-only event (10<sup>th</sup> June 2020) and long time period observation from April to August in 2020. The article ends with a summary and conclusion in section 5.

## 65 2 Location and Instruments Description

### 2.1 Site description

Ny-Ålesund (79 °N, 12 °E), Svalbard, is located in the North Atlantic atmospheric transport gateway to the Arctic. The AWIPEV<sup>2</sup> research base is part of the village Ny-Ålesund, jointly operated by the AWI Potsdam<sup>3</sup> and the IPEV institute<sup>4</sup>. The AWI Potsdam operates an extensive suite of instruments, some of which are a very useful complement to the NYAEM-FTS  
70 (section 2.2), including an aerosol Lidar instrument (section 2.3) and a sun-photometer (section 3.2).

### 2.2 The NYAEM-FTS Instrument

The Fourier Transform spectrometer, NYAEM-FTS, for measuring down-welling emission in the thermal infrared was installed in summer 2019. The NYAEM-FTS consists of a Bruker Vertex 80 Fourier Transform Spectrometer, a SR800 blackbody, an automatically operated mirror to select the radiation source and an automatically operated hutch with shields the instrument  
75 from the environment. It is situated in a temperature stabilized laboratory, at about 21 - 25 °C.

The Bruker Vertex 80 instrument is a table-top instrument. It is operated in zenith geometry with an adjustable field of view in the range of 3.3 to 22 mrad. The beamsplitter is a KBr beam splitter and the detector is an extended MCT detector with the spectral range 400 - 2500 cm<sup>-1</sup> (4 - 25 μm). This instrument measures with a spectral resolution of 0.08 cm<sup>-1</sup> (08.2019 - 08.2020) and 0.3 cm<sup>-1</sup> (08.2020 to present). For the analysis of aerosol properties all resolutions are suitable,  
80 because the spectral features are broadband (compare Fig. 1). The mirror selecting the emission source is the first optical part of the setup, and a total power calibration is performed to gain the radiance from spectra (Revercomb et al., 1988). This means three measurements are required to complete the observation of a spectrum, two measurements of the blackbody at hot and ambient temperature respectively, and one measurement pointing skywards (Rathke and Fischer, 2000; Turner, 2005; Richter et al., 2022). The SR800 blackbody is used as a blackbody radiator. It can be adjusted between 0 and 120 °C, holding the  
85 temperature within 0.1 K.

---

<sup>2</sup>www.awipev.eu

<sup>3</sup>Alfred Wegener Institut; www.awi.de

<sup>4</sup>Polar Institute Paul Emile Victor; www.ipev.fr

Fig. 1 shows four different emission spectra measured by the NYAEM-FTS in clear day, thick cloud, thin cloud and aerosol event respectively. The Planck function at 280 K is also presented in this figure. From Fig. 1, the intensity of thick cloud emission in infrared is high, close to the one calculated from Planck function. However, in the atmospheric window between 800 - 1200  $\text{cm}^{-1}$ , the intensity of clear sky emission is quite lower (close to zero) than that in thick cloud. Between the emission spectra of thick cloud and clear sky in this window (800 - 1200  $\text{cm}^{-1}$ ), an aerosol (Fig. 1 orange line) and a thin cloud (Fig. 1 blue line) emission spectra are presented as well, showing the baseline, from which the aerosol information will be retrieved. In general, it is easy to distinguish the difference between a spectrum of a thick cloud and a clear sky spectrum, however, distinguishing aerosols from a thin cloud is difficult or impossible. Therefore more information from other instruments, e.g. Lidar measurement is used to distinguish days with clouds from days with aerosols present above the instrument.

### 95 2.3 The Raman-Lidar “KARL”

In Ny-Ålesund, a Raman-Lidar “KARL” is operated to measure in 3 colors (355, 532, and 1064 nm) (Ritter et al., 2016). It is positioned about 10 meters away from NYAEM-FTS measurement also pointing skywards. Aerosol backscatter coefficients (in all three colors), extinction coefficients (355 and 532 nm), and depolarization (355 and 532 nm) are measured.

For Lidar products, the aerosol backscatter coefficient ( $\beta^{aer}$ ), the aerosol depolarization ( $\delta^{aer}$ ) and the color ratio ( $CR$ ) are used for aerosol optical property analysis. According to Freudenthaler et al. (2009), the definitions of those quantities are given as follows:

$$\delta^{aer}(\lambda) = \frac{\beta_{\perp}^{aer}(\lambda)}{\beta_{\parallel}^{aer}(\lambda)} \quad (1)$$

$\beta_{\perp}^{aer}(\lambda)$  and  $\beta_{\parallel}^{aer}(\lambda)$  are the backscatter coefficients of the vertical and parallel polarized light, respectively. The depolarization depends on the particles’ shape, e.g. spherical particles do not show any depolarization in the backscatter.

$$105 \quad CR(\lambda_1, \lambda_2) = \frac{\beta_{\lambda_1}^{aer}}{\beta_{\lambda_2}^{aer}} \quad (2)$$

$\beta_{\lambda}^{aer}$  is the aerosol backscatter coefficient at wavelength  $\lambda$ . More details are given in Freudenthaler et al. (2009) and Ritter et al. (2016). Based on that, Ritter et al. (2016) distinguished six conditions for the aerosol classification using those Lidar quantities (compare Tab. 1).

## 3 Methods and Data

### 110 3.1 Retrieval Algorithm TCWRET2-V1 and TCWRET-V2

The retrieval algorithms, TCWRET-V1 and TCWRET-V2, are based on TCWRET developed by Richter et al. (2022). TCWRET-V1 is used for cloud parameter retrieval while TCWRET-V2 is modified for aerosol retrieval. The main difference between the two is the scattering properties look-up table. The core of the retrieval program TCWRET is the radiative transfer model LBLDIS (Richter et al., 2022) which consists of the clear sky radiative transfer model LBLRTM (Clough et al., 2005) and

115 the scattering code DISORT (Stamnes et al., 1988) . The coupled model LBLDIS is used in several retrieval algorithms, such as MIXCRA (Turner, 2005), CLARRA (Rowe et al., 2013), and TCWRET (Richter et al., 2022). Note that these retrieval algorithms share the same forward models. The differences are the particular implementation, e.g. of the scattering.

In this paper, TCWRET-V1 means TCWRET with cloud databases, while TCWRET-V2 means TCWRET with aerosol databases. The algorithm reliability, or how well the method can precisely retrieve aerosol information, has been tested in section 3.1.4. In the Sec. 3.1.1, the aerosol scattering properties look-up tables and artificial spectra simulated using forward model are described in detail. A description of retrieval algorithm can be found in App. A.

### 3.1.1 Aerosol Scattering Properties Look-up Tables

In this study, sulfate, sea salt, dust, and BC are retrieved using the retrieval algorithm, TCWRET-V2. The complex refractive index database only covers the above mentioned aerosols in the infrared band because the spectral signature of the other aerosols is too small and it is not possible to retrieve them from the IR spectra. The complex imaginary refractive index of sulfate and dust are based on OPAC/GADA database, BC from Chang and Charalampopoulos (1990), and sea salt from Eldridge and Palik (1997), and Palik (1997) (compare Fig. 3).

The aerosol optical properties are calculated using the Lorenz-Mie theory. The code for this calculation has been developed by Mishchenko et al. (1999). For aerosol scattering properties calculations, information on the aerosol size distribution as well as their shapes is also needed. In Mie code (Mishchenko et al., 1999), the sphere shape of aerosol with a single-mode log-normal size distribution of particles is selected. The log-normal function is given as follows:

$$n_N(D) = \frac{N}{\sqrt{2\pi D \ln(\sigma_g)}} \exp\left(-\frac{\ln^2(D/D_g)}{\ln^2(\sigma)}\right) \quad (3)$$

Where  $N$  is the total aerosol number concentration  $D_g$  is the median diameter, and  $\sigma_g$  is termed geometric standard deviation. In this study, the geometric standard deviation of size distribution of aerosol is assumed to be 0.2 and the effective radius ( $R_{\text{eff}}$ ) is set from 0.1 to 1  $\mu\text{m}$ . The main reason for setting the upper limit of the  $R_{\text{eff}}$  to 1  $\mu\text{m}$  is that aerosols in the Arctic region is often below 1  $\mu\text{m}$ , according to the measurements of aerosol size distribution in the Arctic area ((Asmi et al., 2016; Park et al., 2020; Boyer et al., 2022)). In addition, if such constraint is not set to 1  $\mu\text{m}$ , occasionally, the retrieval of fine particles, such as sulfate and BC, will be mathematically increased for a better fit of the spectrum, which is artificial. Because sea salt can be larger than 1  $\mu\text{m}$ , when the retrieved  $R_{\text{eff}}$  of sea salt is close to 1  $\mu\text{m}$  and sea salt is the dominant aerosol, the database of sea salt is extended to 2.5  $\mu\text{m}$  and the retrieval is run again.

### 3.1.2 Instruments Joint Observation Scheme

As previously indicated, it is difficult to distinguish between thin clouds and aerosols only relying on the NYAEM-FTS instrument. To select the spectra in aerosol-only scenarios, the measurements of the KARL Lidar are used (compare Sec. 2.3).

The aerosol or cloud height is determined from the KARL Lidar measurement and provided to the retrieval algorithm, TCWRET (compare Sec. 3.1). For cloud-only observations, the first version of retrieval algorithm, Total Cloud Water retrieval (TCWRET-V1), is used to retrieve cloud parameters as described by Richter et al. (2022). For aerosol-only events, the modified

version, TCWRET-V2, is used to do the aerosol components retrieval. For complex situations with simultaneous existence of clouds and aerosols, the concurrent NYAEM-FTS measurements will be excluded. The flow diagram of the joint observation scheme is found in Fig. 2a.

150 The flow diagram in TCWRET-V2 is given in Fig. 2b. As shown in Fig. 2b, there are several inputs for model simulations. Firstly, the databases for scattering coefficients of different aerosol types are calculated using Mie code (Mishchenko et al., 1999) based on aerosol complex refractive index and aerosol size distribution. Secondly, the atmospheric state profile, which includes temperature, humidity, and pressure (referred to as THP), is obtained from ERA5 reanalysis data with a time resolution of 3 hours (Hersbach et al., 2018). The third input is the aerosol height information, which is provided by the KARL Lidar  
155 (Sec. 2.3). To obtain the temperature of the aerosol layer, the fourth input, the ERA5 temperature is interpolated to the altitude measured by the KARL Lidar. Furthermore, for all aerosol types, the a priori information of aerosol is fixed as  $AOD = 0.0001$  and  $R_{\text{eff}} = 0.35 \mu\text{m}$ .

### 3.1.3 Artificial Spectra from LBLDIS

When considering down-welling emission from the atmosphere on a clear day, the main contribution to emission in the thermal  
160 infrared band are from the greenhouse gases, i.e.  $\text{CO}_2$ ,  $\text{H}_2\text{O}$ ,  $\text{N}_2\text{O}$ ,  $\text{CO}$ ,  $\text{CH}_4$  and  $\text{O}_3$ . If there is a cloud or aerosol layer, its broad band emissions can be observed as well (compare Fig. 1).

Several thermal infrared emission spectra from the LBLDIS model are shown in Fig. 4. Under the same number density, different aerosol types exhibit unique characteristics in the infrared emission spectra, shown in Fig. 4a. Among those aerosols, the radiance emitted from sea salt is lowest, due to its smallest light absorbing capability compared to other aerosols. When  
165 the number density is fixed in model simulation, the radiance from sea salt increases with the size of particles (Fig. 4b). Other aerosol types with larger size are presented in Fig. A1. Using the same number density, the radiance from sea salt with the same size as other aerosols is significantly lower; only when sea salt has a large particle size compared to the other aerosols, are the radiances comparable. Figure 4c shows the thermal infrared emission spectra of atmospheric gases (clear sky) and different aerosols within atmosphere. According to Fig. 4c, in some wavebands, the gas emission dominates over the aerosol signal.  
170 Those bands are not considered for the retrieval, e.g.  $\text{CO}_2$  in  $640 - 690 \text{ cm}^{-1}$  and  $\text{O}_3$  in  $1000 - 1100 \text{ cm}^{-1}$ . Aerosol windows (compare Fig. A2) are chosen in the region in  $500 - 600 \text{ cm}^{-1}$ ,  $800 - 1000 \text{ cm}^{-1}$ , and  $1100 - 1200 \text{ cm}^{-1}$ , which are selected as retrieval micro-windows (vertical lines in Fig. 4c). The spectra in Fig. 4d are shown in the form of the difference between the aerosol and clear sky in those micro-windows. Based on that, the emission spectra in aerosol events are different from each other, which means the emission from aerosols can be measured and aerosol types can be retrieved using the emission  
175 FTS. The reason for avoiding the gas emissions is the dependency of the gas emissions on the temperature distribution in the atmosphere.

### 3.1.4 Error estimation

In order to investigate the precision of the retrieved values, artificial spectra simulated from LBLDIS are used to explore the performance of TCWRET-V2 in the retrieval of aerosol types. Artificial spectra with preset values of AOD as well as  $R_{\text{eff}}$  are

180 created using LBLDIS and then act as measured spectra retrieved by the algorithm. Specifically, we assume that all particles are concentrated on a single level, 2000 m above surface ground. The AOD's of sea salt, sulfate, dust and BC are set 0.1, respectively, with  $R_{\text{eff}}$  of 0.7  $\mu\text{m}$ . The retrieval results suffer from several uncertainty sources:

- Uncertainty of the aerosol height, which is similar to the error of aerosol layer temperature. In this study, the aerosol height is given by Lidar measurement.
- 185 – Uncertainty of the humidity profile has a significant signal on the far-infrared emission spectrum, at about 1500 - 2000  $\text{cm}^{-1}$ . Thus, the water vapor profile could change the radiance of emission spectrum, which might affect the results of retrieval.
- Calibration uncertainty in the measured spectra is also an important uncertainty in the retrieval, which could be caused by misreading of the blackbody temperature. In this study, the total power calibration method (Revercomb et al., 1988) is used to calibrate the spectra. Assuming the accuracy of the blackbody temperature is  $\Delta T_{BB} = \pm 1K$ . The propagation of this error into radiance is

$$\Delta L = \sqrt{\left(\frac{\partial L_{\text{atm}}}{\partial T_{BB}} \cdot 1K\right)^2} \quad (4)$$

According to Richter et al. (2022), the partial derivative  $\frac{\partial L_{\text{atm}}}{\partial T_{BB}}$  can be estimated using:

$$L_{\text{atm}} = B(T_{\text{amb}}) + 0.2 \cdot (B(T_{\text{hot}}) - B(T_{\text{amb}})) \quad (5)$$

195 where  $B(T_{\text{hot}})$  means hot blackbody temperature and  $B(T_{\text{amb}})$  means surface air temperature. With  $T_{\text{hot}} = 100\text{ }^\circ\text{C}$  and  $T_{\text{amb}} = 0\text{ }^\circ\text{C}$ ,  $\frac{\partial L_{\text{atm}}}{\partial T_{BB}} \cdot 1K = 0.41\text{mWsr}^{-1}\text{m}^{-2}\text{cm}^{-1}$  is an average for the spectral interval between 500 and 2000  $\text{cm}^{-1}$ .

- Measurement uncertainty. The noise on the spectrum is assumed to be white in space and time.
- Database uncertainty could be caused by uncertainty of aerosol complex refractive index. Both the real and imaginary part could have an influence on the accuracy of aerosol scattering properties look-up tables, as we mentioned in Sec. 3.1.1.

200 The artificial spectra with modifications are performed according Tab. 2. Compared with preset values, one can then compute the difference between retrieved values with preset values by perturbing each parameter.

### 3.2 AOD in AERONET and MERRA-2

The dataset, AErosol RObotic NETwork (AERONET), provides aerosol products primarily in the visible waveband. Additionally, Modern-Era Retrospective analysis for Research and Applications version 2 (MERRA-2) provides aerosol information. Hence, it is worth investigating whether our measurements can be combined with existing data to provide more comprehensive aerosol information in the future. In this paper, we summarize the results from AERONET and MERRA-2 in the aerosol case for providing a general understanding of the aerosol events (compare Fig. 8).

The AERONET project is a federation of ground-based remote sensing aerosol networks. It is widely used as a ground-  
210 based reference for validation of aerosol retrievals. In Ny-Ålesund, a Sun-photometer measuring solar extinction at several  
wavelengths is adopted to give the daily variance of AOD on 10<sup>th</sup> of June 2020.

MERRA-2 is the latest version of the global atmospheric reanalysis dataset produced by NASA Global Modeling and  
Assimilation Office (GMAO) using the Goddard Earth Observing System Model (GEOS) version 5.12.4. An hourly time-  
averaged 2-dimensional data collection (M2T1NXAER) in MERRA-2 is used in this study (Gelaro et al., 2017). This collection  
215 consists of assimilated aerosol diagnostics, such as column mass density of aerosol components (BC, dust, sea salt, sulfate,  
and organic carbon), surface mass concentration of aerosol components, and total extinction (and scattering) AOD at 550 nm.  
The dataset covers the period of 1980 to present. In this paper, the AOD of sea salt, sulfate, dust, BC and organic carbon in  
Ny-Ålesund are shown on 10<sup>th</sup> of June 2020.

## 4 Results

### 220 4.1 Artificial Spectra Retrieval

As we mentioned in Sec. 3.1.4, the artificial spectra are given by forward model with preset values (compare Tab. 2). The  
retrieved results of those artificial spectra can be obtained by using the artificial spectra as the observed spectra in the retrieval  
algorithm. The difference between retrieved values with preset values by perturbing each parameter is shown in Fig. 5.

Fig. 5a shows that the original case, without any modifications is close to the preset values. The difference of AOD retrieved  
225 in the original case with preset values are less than 0.005 at 900 cm<sup>-1</sup>, leading to convincing results using this retrieval  
algorithm. Noise in the measurements and water vapor profiles have small effects on the retrieval. The most important parameter  
is the database error, caused by the uncertainty of the complex refractive index. A decrease of 10% in the real part of the  
complex refractive index will cause about 7% positive errors in AOD of sulfate, dust and BC, except for AOD of sea salt,  
which shows 18% negative error. While the 10% decrease of the imaginary part of the complex refractive index will cause  
230 about 4% negative errors in AOD of sulfate, dust and BC and 1% negative error in AOD of sea salt. Following the databases  
errors, the second most important error is the calibration error, e.g. 1 K misreading of the temperature of the blackbody will  
cause a change in radiance of about 0.47 mW<sub>sr</sub><sup>-1</sup>m<sup>-2</sup>cm<sup>-1</sup>. An offset of radiance by 1 mW<sub>sr</sub><sup>-1</sup>m<sup>-2</sup>cm<sup>-1</sup> causes an error  
of about 4% overestimation in the results. The temperature error of the aerosol layer is the third most important effect in the  
aerosol retrieval.

235 In order to show the reliable range of the retrieved AOD, using similar artificial spectra but for several AOD from 0.001 to 0.1  
at 900 cm<sup>-1</sup>, the relative uncertainties of AOD in original cases with those preset values are given in Fig. 5b. The uncertainty  
of the AOD retrieval is 0.0015, hence aerosols are reliably retrieved when the AOD is > 0.003. Therefore, we consider the  
results to be reliable when the retrieved AOD is greater than 0.003.

Organic carbon (OC) is one of the major components in tropospheric aerosols. It is not considered because there are no data  
240 of the complex refractive index in the infrared waveband of OC. There are also many types of OC, each of them has a different  
spectral signature. We assume, that the spectral signature of OC is very weak. However if there are spectral features which are

not fitted, e.g. due to the presence of aerosol types not accounted for in the scattering database, the error margin on the retrieved aerosol types will be increased.

In conclusion, when aerosol is present in the atmosphere, the emission from aerosol can be measured by FTS. According to forward model simulations, different aerosol types show their own features. Using artificial spectra with preset values, error estimations caused by the retrieval could be calculated.

## 4.2 Aerosol-only Retrieval

On the 10<sup>th</sup> of June 2020 there was a distinct aerosol event in Ny-Ålesund (compare Fig. 6, showing the aerosol distribution derived using the KARL Lidar). This aerosol event is chosen as our aerosol-only case. Figure 7 presents the four different aerosol classes and cloud based on the Lidar classification method (compare Sec.2.3). During this day, aerosols are mainly distributed below 1500 m (compare Fig. 6). From 7:00 to 11:00, the thickness of a coarse aerosol layer (dense aerosol in Lidar classification method in Sec. 2.3) near the surface decreases, while in the afternoon, this aerosol load increases and splits into two layers, one near the surface and another, activated aerosol, appears at the height of about 500 m. At around 8:00 clouds are present in a height of 3500 m, which has been screened out in the aerosol-only FTS retrieval.

Figure 7 shows the results retrieved from the FTS. From Fig. 7a, the dominant aerosol is sulfate above Ny-Ålesund, about  $AOD = 0.007 \pm 0.0027$  in daily average. Dust also exists but lower than sulfate for most of the time, about  $AOD = 0.0039 \pm 0.0029$  for daily average. The AOD of BC and sea salt are much lower than the reliable range of AOD, therefore, the retrieved values of BC and sea salt are not presented. From 9:00 to 11:00, the AOD of sulfate decreases with time. After that, it increases slowly from 12:00 to 14:00, about 0.0135 at 14:00. Compared with sulfate, dust as a second dominant aerosol does not show a significant daily variation as sulfate. From the long time period observation, dust and sulfate are independent in the retrieval (compare Fig. 9), which will be discussed in the following section. Considering the uncertainty of dust and the reliable range of the retrieval, it can be concluded that the AOD of dust is relatively stable during that day. From Fig. 7b, both sulfate and dust are small in size,  $0.25 \pm 0.03 \mu\text{m}$  and  $0.30 \pm 0.06 \mu\text{m}$ , respectively.

Figure 8 shows the AOD from the FTS, AERONET and MERRA-2. In this analysis, the AOD from FTS will be called  $AOD_{IR}$ , the AOD from AERONET  $AOD_{AERO}$  and the AOD from MERRA-2 will be written as  $AOD_{MERRA-2}$ . From the measurement of the Sun-photometer (AERONET), as shown in Fig. 8a, the  $AOD_{AERO}$  (blue line for 500 nm and red line for 780 nm) decreases from 8:00 to 11:00 and increases after 14:24. Compared with AERONET,  $AOD_{IR}$  (black line) shows similar daily variation, while the minimum in  $AOD_{MERRA-2}$  (orange line) is at 08:00, about 3 hours earlier than  $AOD_{IR}$  and  $AOD_{AERO}$ . According to MERRA-2 reanalysis data, as shown in Fig. A1b, the first two major aerosol components are sulfate and dust, which is consistent with  $AOD_{IR}$  in Fig. 8. Furthermore, the daily variation of  $AOD_{MERRA-2}$  on the 10<sup>th</sup> of June 2020 is mainly caused by sulfate and sea salt. Apart from sea salt, which shows limited signal in the infrared waveband, the daily variation of sulfate in MERRA-2 is also similar to the FTS measurement, but the turning point in MERRA-2 is about 3 hours earlier than the one in the observations. In conclusion, the agreement of daily variation between FTS measurements and sun-photometer and the consistent in dominant aerosol components between FTS and MERRA-2 reanalysis data show the good quality in the retrieval results of FTS.

Additionally, in the afternoon, from Lidar measurement (compare Fig. 6), there are indications of activated aerosol at the height of about 500 m. In the FTS retrieval algorithm, the databases of aerosol do not include liquid water or activated particles, which means only dry particles are considered in our retrieval. The appearance of an activated aerosol signal indicates that hygroscopic growth of aerosol needs to be considered in the aerosol scattering properties look-up tables, which will be the  
280 focus of future research.

### 4.3 Long Time period Observation

For continuous long-term observation of aerosols, Cloudnet (Illingworth et al., 2007) is a better alternative to the "KARL" Lidar measurement due to its improved data continuity and inclusion of aerosol height data and cloud type information. With the Cloudnet dataset, aerosol-only situations can be distinguished and the corresponding spectra are retrieved using TCWRET-  
285 V2. The results are presented in Fig. 9. The dominant aerosol type varies from April to August and is not fixed. For sulfate, it is often present in the Arctic, higher during Spring time and lower in Summer. Similarly, BC is also frequently observed in the Arctic, with less obvious seasonal variations than that of sulfate. A BC outburst event is observed in each Spring and Summer. In Spring, sulfate and BC are significant while sea salt and dust are lower. In addition, a sea salt enhancement event is observed in Summer, which might be emitted from open water nearby. Fig. 9b - g present correlation plots between different aerosol  
290 types. None of them show a clear correlation, so they can be retrieved independent of each other.

## 5 Conclusions

An FTS instrument, NYAEM-FTS, for measuring down-welling emitted radiation is operated since 2019. Combining with the Raman-Lidar KARL, aerosols can be observed more comprehensively than by either instrument alone.

For the FTS emission measurements, according to forward model simulation, the aerosol signatures of different aerosol  
295 types in the infrared spectral region are quite clear and independent. The retrieval algorithm TCWRET-V1 (Richter et al., 2022) has been modified for retrieval of optical depth and  $R_{\text{eff}}$  of different aerosol types. Combined Lidar and FTS, a scheme of instruments joint measurement is designed and applied to do aerosol component retrieval. The measurements from both instruments in a case study is analyzed on 10<sup>th</sup> of June 2020 (aerosol-only case) to show the potential synergy.

In the aerosol-only case study, 10<sup>th</sup> of June 2020, the signal of cloud and aerosols could be distinguished clearly using  
300 measurements from the Lidar KARL. From the emission FTS measurement we see that sulfate is the dominant aerosol during the whole day. Comparing with sun-photometer measurements, the daily variation of aerosol AOD is mainly effected by sulfate in the infrared. Comparing the results from NYAEM-FTS with MERRA-2 reanalysis data, the proportions of sulfate, dust and BC show good agreement.

For long time period observations from April to August 2020, sulfate is often present in the Arctic, higher during Spring time  
305 and relatively lower in Summer. Similarly, BC is also frequently observed in the Arctic, with less obvious seasonal variations than that of sulfate. During the Spring time, sulfate and BC are significant while sea salt and dust abundances are relatively low. None of them show a clear correlation, so they can be retrieved independent of each other.

The database used in TCWRET-V2 does not include activated particles, which will be subject of a future study.

310 *Code and data availability.* The latest version of TCWRET can be downloaded from GitHub (<https://github.com/RichterIUP/Total-Cloud-Water-retrieval>). The Lidar data, spectra measured from the Emission FTS and retrieval results are available from the corresponding author upon request.

## Appendix A: Description of the retrieval in TCWRET

315 The retrieval method adopted in modified TCWRET for the aerosol case is an optimal estimation method (Rodgers, 2000), the relationship between a measured emission spectrum  $\mathbf{y}$  and unknown aerosol state  $\mathbf{x}$  can be described by a simple mathematical model, as follows:

$$\mathbf{y} = \mathbf{F}(\mathbf{x}) + \varepsilon \quad (\text{A1})$$

where  $\mathbf{F}(\mathbf{x})$  is the forward model and  $\varepsilon$  is the error of observation. The solution of the inverse problem is the state  $\mathbf{x}$  minimizing a cost function  $\xi^2(\mathbf{x})$  usually defined as:

$$\xi^2(\mathbf{x}) = [\mathbf{y} - \mathbf{F}(\mathbf{x})]^T \mathbf{S}_y^{-1} [\mathbf{y} - \mathbf{F}(\mathbf{x})] + [\mathbf{x}_a - \mathbf{x}] \mathbf{S}_a^{-1} [\mathbf{x}_a - \mathbf{x}] \quad (\text{A2})$$

320 where  $\mathbf{S}_y^{-1}$  is the inverse measurement error covariance matrix, containing the variances of the spectral radiance;  $\mathbf{x}_a$  is the a priori;  $\mathbf{S}_a^{-1}$  is the inverse error of the a priori covariance matrix  $\mathbf{x}_a$ ; The state vector  $\mathbf{x}$  in modified TCWRET is defined as follows:  $\mathbf{x} = (\tau_{seasalt}, \tau_{sulfate}, \tau_{dust}, \tau_{BC}, r_{seasalt}, r_{sulfate}, r_{dust}, r_{BC})$ ,  $\tau$  means AOD of aerosols, and  $r$  means  $R_{eff}$  of aerosols.

325 Since the forward model is a non-linear function, an iterative method is needed to minimize the cost function  $\xi^2(\mathbf{x})$ , given as follow:

$$\mathbf{x}_{n+1} = \mathbf{x}_n + \mathbf{s}_n \quad (\text{A3})$$

330 Here  $\mathbf{x}_n$  and  $\mathbf{x}_{n+1}$  are the aerosol parameters of the  $n$ -th and  $(n+1)$ -th step, and  $\mathbf{s}_n$  is the modification of the aerosol parameters during the  $n$ -th iteration. For weak non-linear problems, the Gauss-Newton (GN) method can be successfully applied, while in significant non-linear situations, the GN method is not guaranteed to decrease the cost function, therefore the method of steepest descent could be used. The Levenberg-Marquardt method modification combines both methods by starting with the deepest descent method far away from the minimum and using the GN method near the minimum. At each iteration, a damping factor  $\mu$  is adjusted in such a way that if the step results in a decrease in the cost-function, the damping factor  $\mu$  is decreased, bringing the next step closer to the GN step. If the step causes the cost function to increase, the iteration is repeated with a higher damping factor  $\mu$ , resulting in a step closer to the gradient descent direction Ceccherini and Ridolfi (2010). The adjustment vector  $\mathbf{s}_n$  could be determined by the governing equation, as follows:

$$(\mathbf{K}_n^T \mathbf{S}_y^{-1} \mathbf{K}_n + \mathbf{S}_a^{-1} + \mu^2 \mathbf{S}_a^{-1}) \mathbf{s}_n = \mathbf{K}_n^T \mathbf{S}_y^{-1} [\mathbf{y} - \mathbf{F}(\mathbf{x}_n)] + \mathbf{S}_a^{-1} \cdot (\mathbf{x}_a - \mathbf{x}_n) \quad (\text{A4})$$

340  $\mathbf{K} = \left( \frac{\partial \mathbf{F}(\mathbf{x}_i)_n}{\partial \mathbf{x}_i} \right)$  is the jacobian matrix,  $i$  means parameters in the state vector;  $\mathbf{S}_y^{-1} = \text{diag}(\sigma_i^{-1})$  is the inverse measurement error covariance matrix, containing the variances of the spectral radiance;  $\mathbf{x}_a$  is the a priori;  $\mathbf{S}_a^{-1}$  is the inverse error of the a priori covariance matrix  $\mathbf{x}_a$ ;  $\mu^2 \cdot \mathbf{S}_a^{-1}$  is the Levenberg-Marquardt (LM) term, as we mentioned before.  $\mathbf{F}(\mathbf{x}_i)$  is the calculated spectral radiance and  $\mathbf{y}$  is the measured spectral radiance.

The iteration is said to have converged, if the cost function  $\xi^2$  does not change anymore, i.e. the change in the cost function  $\xi$  is below a threshold. This threshold is set 0.001 in this study, i.e. the iteration has converged if

$$\frac{\xi^2(\mathbf{x}_{n+1}) - \xi^2(\mathbf{x}_n)}{\xi^2(\mathbf{x}_n)} < 0.001 \quad (\text{A5})$$

### A0.1 Averaging Kernels

345 The averaging kernels are a useful diagnostic tool to characterize the solution of the retrieval. In TCWRET, averaging kernels are calculated via

$$\mathbf{A} = \frac{\partial \mathbf{x}_r}{\partial \mathbf{x}} = \frac{\partial \mathbf{x}_r}{\partial \mathbf{y}} \frac{\partial \mathbf{y}}{\partial \mathbf{x}} = \mathbf{T}_r \cdot \mathbf{K}_r \quad (\text{A6})$$

where  $\mathbf{x}_r$  is the retrieved state vector;  $\mathbf{x}$  is the true value of state vector;  $\mathbf{T}_r$  is the final transfer matrix  $\mathbf{T}$  and  $\mathbf{K}_r$  is the final jacobian matrix. According to Ceccherini and Ridolfi (2010), the final transfer matrix could be calculated as follows:

$$350 \begin{cases} \mathbf{T}_0 = \mathbf{0} \\ \mathbf{T}_{n+1} = \mathbf{G}_n + (\mathbf{I} - \mathbf{G}_n \mathbf{K}_n - \mathbf{M}_n \mathbf{S}_a^{-1}) \mathbf{T}_n \\ \mathbf{G}_n = \mathbf{M}_n \mathbf{K}_n^T \mathbf{S}_y^{-1} \\ \mathbf{M}_n = (\mathbf{K}_n^T \mathbf{S}_y^{-1} \mathbf{K}_n + \mathbf{S}_a^{-1} + \mu^2 \mathbf{D}_n)^{-1} \end{cases} \quad (\text{A7})$$

where  $\mathbf{0}$  is a zero matrix and  $\mathbf{I}$  is an identity matrix, other quantities are described before. The matrices  $\mathbf{K}_n$  are calculated in Eq. A4. The calculation of the transfer matrix is performed in parallel to the minimisation. An example of averaging kernels is given as follows:

$$\mathbf{A} = \begin{pmatrix} \tau_{SS} & \tau_{SO4} & \tau_{Dust} & \tau_{BC} & Reff_{SS} & Reff_{SO4} & Reff_{Dust} & Reff_{BC} \\ 0.280 & -0.099 & 0.264 & 0.232 & 0.093 & -0.046 & 0.014 & 0.073 \\ -0.057 & 0.940 & 0.047 & 0.042 & -0.067 & 0.057 & 0.026 & 0.020 \\ 0.006 & 0.006 & 0.585 & 0.036 & -0.007 & -0.040 & 0.151 & -0.022 \\ 0.172 & 0.178 & 0.163 & 0.171 & 0.030 & -0.011 & 0.023 & 0.065 \\ 0.248 & -0.134 & 0.268 & 0.250 & 0.112 & -0.042 & 0.075 & 0.063 \\ 0.000 & 0.000 & 0.000 & 0.000 & 0.000 & 0.000 & 0.000 & 0.000 \\ 0.012 & 0.025 & 1.354 & 0.102 & -0.023 & -0.075 & 0.414 & -0.051 \\ 0.149 & 0.177 & 0.195 & 0.190 & 0.045 & -0.014 & 0.062 & 0.061 \end{pmatrix} \begin{matrix} \tau_{SS} \\ \tau_{SO4} \\ \tau_{Dust} \\ \tau_{BC} \\ Reff_{SS} \\ Reff_{SO4} \\ Reff_{Dust} \\ Reff_{BC} \end{matrix}$$

355 The averaging kernels belong to the retrieved result, because they include much information about the retrieval results, e.g. how  
much influence is exerted by the a priori and how independent the retrieved quantities are from each other. On the diagonal  
elements one finds the derivatives of each element in the retrieved state vector with respect to its corresponding element in  
the true state vector. From the averaging kernel, the AOD of sulfate is the parameter least dependent on a priori information,  
followed by the AOD of dust and sea salt. Except for dust, all other aerosol size information is difficult to be retrieved. Besides,  
360 the information in each row or column suggests that there is very little connection between the parameters and that they are all  
independent of each other, supporting the finding of the low correlation in sec. 4.3.

*Author contributions.* PR implemented TCWRET and DJ developed it into the retrieval of aerosol parameters using TCWRET. MP designed  
and built the measurement setup, performed measurements and gave advice in the development of TCWRET. CR performed Lidar measure-  
ments and gave advice in using the Lidar data and the sun-photometer data. XS gave advice in forward model simulation. MB gave advice  
365 on the calibration processes, performed the measurements and maintained the instrument. JN gave advice in the setup of the measurement  
and the development of TCWRET. All authors contributed to the manuscript.

*Competing interests.* The authors declare no competing interests

*Acknowledgements.* We gratefully acknowledge the funding by the Deutsche Forschungsgemeinschaft (DFG, German Research Foundation)  
–Project nummer 268020496 – TRR 172 , within the Transregional Collaborative Research Center “Arctic Amplification: Climate Relevant  
370 Atmospheric and SurfaCe Processes, and Feedback Mechanisms ((AC)<sup>3</sup>)”, in sub-project E02: Ny-Ålesund Column Thermodynamic Struc-  
ture, Clouds, Aerosols, Trace Gases and Radiative Effects. We thank the AWI Bremerhaven and the AWI Potsdam for logistical support on  
the AWIPEV research base and the station personnel for on-site support. We thank he senate of Bremen for partial funding of this work.

## References

- Abbatt, J. P. D., Leaitch, W. R., Aliabadi, A. A., Bertram, A. K., Blanchet, J.-P., Boivin-Rioux, A., Bozem, H., Burkart, J., Chang, R.  
375 Y. W., Charette, J., Chaubey, J. P., Christensen, R. J., Cirisan, A., Collins, D. B., Croft, B., Dionne, J., Evans, G. J., Fletcher, C. G., Galí,  
M., Ghahremaninezhad, R., Girard, E., Gong, W., Gosselin, M., Gourdal, M., Hanna, S. J., Hayashida, H., Herber, A. B., Hesarakı, S.,  
Hoor, P., Huang, L., Husserr, R., Irish, V. E., Keita, S. A., Kodros, J. K., Köllner, F., Kolonjari, F., Kunkel, D., Ladino, L. A., Law, K.,  
Levasseur, M., Libois, Q., Liggio, J., Lizotte, M., Macdonald, K. M., Mahmood, R., Martin, R. V., Mason, R. H., Miller, L. A., Moravek,  
A., Mortenson, E., Mungall, E. L., Murphy, J. G., Namazi, M., Norman, A.-L., O'Neill, N. T., Pierce, J. R., Russell, L. M., Schneider, J.,  
380 Schulz, H., Sharma, S., Si, M., Staebler, R. M., Steiner, N. S., Thomas, J. L., von Salzen, K., Wentzell, J. J. B., Willis, M. D., Wentworth,  
G. R., Xu, J.-W., and Yakobi-Hancock, J. D.: Overview paper: New insights into aerosol and climate in the Arctic, *Atmos. Chem. Phys.*,  
19, 2527–2560, <https://doi.org/10.5194/acp-19-2527-2019>, 2019.
- Asmi, E., Kondratyev, V., Brus, D., Laurila, T., Lihavainen, H., Backman, J., Vakkari, V., Aurela, M., Hatakka, J., Viisanen, Y., Uttal, T.,  
Ivakhov, V., and Makshtas, A.: Aerosol size distribution seasonal characteristics measured in Tiksi, Russian Arctic, *Atmos. Chem. Phys.*,  
385 16, 1271–1287, <https://doi.org/10.5194/acp-16-1271-2016>, 2016.
- Bond, T. C., Doherty, S. J., Fahey, D. W., Forster, P. M., Berntsen, T., DeAngelo, B. J., Flanner, M. G., Ghan, S., Kärcher, B., Koch, D.,  
et al.: Bounding the role of black carbon in the climate system: A scientific assessment, *J. Geophys. Res.: Atmos.*, 118, 5380–5552,  
<https://doi.org/10.1002/jgrd.50171>, 2013.
- Bony, S., Colman, R., Kattsov, V. M., Allan, R. P., Bretherton, C. S., Dufresne, J.-L., Hall, A., Hallegatte, S., Holland, M. M., Ingram, W.,  
390 Randall, D. A., Soden, B. J., Tselioudis, G., and Webb, M. J.: How Well Do We Understand and Evaluate Climate Change Feedback  
Processes?, *J. Clim.*, 19, 3445 – 3482, <https://doi.org/10.1175/JCLI3819.1>, 2006.
- Boyer, M., Aliaga, D., Pernov, J. B., Angot, H., Quéléver, L. L. J., Dada, L., Heutte, B., Dall'Osto, M., Beddows, D. C. S., Brasseur, Z., Beck,  
I., Bucci, S., Duetsch, M., Stohl, A., Laurila, T., Asmi, E., Massling, A., Thomas, D. C., Nøjgaard, J. K., Chan, T., Sharma, S., Tunved,  
P., Krejci, R., Hansson, H. C., Kulmala, M., Petäjä, T., Sipilä, M., Schmale, J., and Jokinen, T.: A full year of aerosol size distribution  
395 data from the central Arctic under an extreme positive Arctic Oscillation: Insights from the MOSAiC expedition, *Atmos. Chem. Phys.*  
*Discuss.*, 2022, 1–45, <https://doi.org/10.5194/acp-2022-591>, 2022.
- Ceccherini, S. and Ridolfi, M.: Technical Note: Variance-covariance matrix and averaging kernels for the Levenberg-Marquardt solution of  
the retrieval of atmospheric vertical profiles, *Atmos. Chem. Phys.*, 10, 3131–3139, <https://doi.org/10.5194/acp-10-3131-2010>, 2010.
- Chang, H.-c. and Charalampopoulos, T.: Determination of the wavelength dependence of refractive indices of flame soot, *Proc. R. Soc.*  
400 *London, Ser. A*, 430, 577–591, <https://doi.org/10.1098/rspa.1990.0107>, 1990.
- Clough, S., Shephard, M., Mlawer, E., Delamere, J., Iacono, M., Cady-Pereira, K., Boukabara, S., and Brown, P.: Atmo-  
spheric radiative transfer modeling: a summary of the AER codes, *J. Quant. Spectrosc. Radiat. Transfer*, 91, 233–244,  
<https://doi.org/https://doi.org/10.1016/j.jqsrt.2004.05.058>, 2005.
- Domine, F., Sparapani, R., Ianniello, A., and Beine, H. J.: The origin of sea salt in snow on Arctic sea ice and in coastal regions, *Atmos.*  
405 *Chem. Phys.*, 4, 2259–2271, <https://doi.org/10.5194/acp-4-2259-2004>, 2004.
- Donth, T., Jäkel, E., Ehrlich, A., Heinold, B., Schacht, J., Herber, A., Zanatta, M., and Wendisch, M.: Combining atmospheric and snow  
radiative transfer models to assess the solar radiative effects of black carbon in the Arctic, *Atmos. Chem. Phys.*, 20, 8139–8156,  
<https://doi.org/10.5194/acp-20-8139-2020>, 2020.

- Eldridge, J. and Palik, E. D.: - Sodium Chloride (NaCl), in: Handbook of Optical Constants of Solids, edited by Palik, E. D., pp. 775–793, Academic Press, Burlington, <https://doi.org/https://doi.org/10.1016/B978-012544415-6.50041-8>, 1997.
- Francis, D., Eayrs, C., Chaboureaud, J.-P., Mote, T., and Holland, D. M.: Polar jet associated circulation triggered a Saharan cyclone and derived the poleward transport of the African dust generated by the cyclone, *J. Geophys. Res.: Atmos.*, 123, 11–899, <https://doi.org/10.1029/2018JD029095>, 2018.
- Francis, D., Eayrs, C., Chaboureaud, J.-P., Mote, T., and Holland, D. M.: A meandering polar jet caused the development of a Saharan cyclone and the transport of dust toward Greenland, *Advances in Science and Research*, 16, 49–56, <https://doi.org/10.5194/asr-16-49-2019>, 2019.
- Freudenthaler, V., Esselborn, M., Wiegner, M., Heese, B., Tesche, M., Ansmann, A., Müller, D., Althausen, D., Wirth, M., Fix, A., Ehret, G., Knippertz, P., Toledano, C., Gasteiger, J., Garhammer, M., and Seefeldner, M.: Depolarization ratio profiling at several wavelengths in pure Saharan dust during SAMUM 2006, *Tellus B*, 61, 165–179, <https://doi.org/10.1111/j.1600-0889.2008.00396.x>, 2009.
- Gelaro, R., McCarty, W., Suárez, M. J., Todling, R., Molod, A., Takacs, L., Randles, C. A., Darmenov, A., Bosilovich, M. G., Reichle, R., Wargan, K., Coy, L., Cullather, R., Draper, C., Akella, S., Buchard, V., Conaty, A., da Silva, A. M., Gu, W., Kim, G.-K., Koster, R., Lucchesi, R., Merkova, D., Nielsen, J. E., Partyka, G., Pawson, S., Putman, W., Rienecker, M., Schubert, S. D., Sienkiewicz, M., and Zhao, B.: The Modern-Era Retrospective Analysis for Research and Applications, Version 2 (MERRA-2), *J. Clim.*, 30, 5419 – 5454, <https://doi.org/10.1175/JCLI-D-16-0758.1>, 2017.
- Graversen, R. G., Langen, P. L., and Mauritsen, T.: Polar Amplification in CCSM4: Contributions from the Lapse Rate and Surface Albedo Feedbacks, *J. Clim.*, 27, 4433 – 4450, <https://doi.org/10.1175/JCLI-D-13-00551.1>, 2014.
- Hersbach, H., Bell, B., Berrisford, P., Biavati, G., Horányi, A., Muñoz Sabater, J., Nicolas, J., Peubey, C., Radu, R., Rozum, I., Schepers, D., Simmons, A., Soci, C., Dee, D., and Thépaut, J.-N.: ERA5 hourly data on pressure levels from 1979 to present, Copernicus climate change service (c3s) climate data store (cds). (Accessed on < 01-12-2022 >), 10, <https://doi.org/10.24381/cds.bd0915c6>, 2018.
- Illingworth, A. J., Hogan, R. J., E., O., Bouniol, D., Brooks, M. E., Delanoé, J., Donovan, D. P., Eastment, J. D., Gaussiat, N., Goddard, J. W. F., Haefelin, M., Baltink, H. K., Krasnov, O. A., Pelon, J., Piriou, J.-M., Protat, A., Russchenberg, H. W. J., Seifert, A., Tompkins, A. M., van Zadelhoff, G.-J., Vinit, F., Willén, U., Wilson, D. R., and Wrench, C. L.: Cloudnet: Continuous Evaluation of Cloud Profiles in Seven Operational Models Using Ground-Based Observations, *Bull. Am. Meteorol. Soc.*, 88, 883–898, 2007.
- Koch, D., Bauer, S. E., Genio, A. D., Faluvegi, G., McConnell, J. R., Menon, S., Miller, R. L., Rind, D., Ruedy, R., Schmidt, G. A., and Shindell, D.: Coupled Aerosol-Chemistry–Climate Twentieth-Century Transient Model Investigation: Trends in Short-Lived Species and Climate Responses, *J. Clim.*, 24, 2693 – 2714, <https://doi.org/10.1175/2011JCLI3582.1>, 2011.
- Kodros, J. K., Hanna, S. J., Bertram, A. K., Leaitch, W. R., Schulz, H., Herber, A. B., Zanatta, M., Burkart, J., Willis, M. D., Abbatt, J. P. D., and Pierce, J. R.: Size-resolved mixing state of black carbon in the Canadian high Arctic and implications for simulated direct radiative effect, *Atmos. Chem. Phys.*, 18, 11 345–11 361, <https://doi.org/10.5194/acp-18-11345-2018>, 2018.
- Krinner, G., Boucher, O., and Balkanski, Y.: Ice-free glacial northern Asia due to dust deposition on snow, *Climate Dynamics*, 27, 613–625, <https://doi.org/10.1007/s00382-006-0159-z>, 2006.
- Lee, S.-M., Shi, H., Sohn, B.-J., Gasiewski, A. J., Meier, W. N., and Dybkjær, G.: Winter Snow Depth on Arctic Sea Ice From Satellite Radiometer Measurements (2003–2020): Regional Patterns and Trends, *Geophys. Res. Lett.*, 48, e2021GL094541, <https://doi.org/https://doi.org/10.1029/2021GL094541>, e2021GL094541 2021GL094541, 2021.
- May, N., Quinn, P., McNamara, S., and Pratt, K.: Multiyear study of the dependence of sea salt aerosol on wind speed and sea ice conditions in the coastal Arctic, *J. Geophys. Res.: Atmos.*, 121, 9208–9219, <https://doi.org/10.1002/2016JD025273>, 2016.

- Ming, J., Xiao, C., Cachier, H., Qin, D., Qin, X., Li, Z., and Pu, J.: Black Carbon (BC) in the snow of glaciers in west China and its potential effects on albedos, *Atmos. Res.*, 92, 114–123, <https://doi.org/https://doi.org/10.1016/j.atmosres.2008.09.007>, 2009.
- Mishchenko, M. I., Dlugach, J. M., Yanovitskij, E. G., and Zakharova, N. T.: Bidirectional reflectance of flat, optically thick particulate layers: an efficient radiative transfer solution and applications to snow and soil surfaces, *Journal of Quantitative Spectroscopy and Radiative Transfer*, 63, 409–432, [https://doi.org/https://doi.org/10.1016/S0022-4073\(99\)00028-X](https://doi.org/https://doi.org/10.1016/S0022-4073(99)00028-X), 1999.
- 450 Palik, E. D.: - Gallium Arsenide (GaAs), in: *Handbook of Optical Constants of Solids*, edited by Palik, E. D., pp. 429–443, Academic Press, Burlington, <https://doi.org/https://doi.org/10.1016/B978-012544415-6.50018-2>, 1997.
- Park, J., Dall'Osto, M., Park, K., Gim, Y., Kang, H. J., Jang, E., Park, K.-T., Park, M., Yum, S. S., Jung, J., Lee, B. Y., and Yoon, Y. J.: Shipborne observations reveal contrasting Arctic marine, Arctic terrestrial and Pacific marine aerosol properties, *Atmos. Chem. Phys.*, 20, 5573–5590, <https://doi.org/10.5194/acp-20-5573-2020>, 2020.
- 455 Philipp, D., Stengel, M., and Ahrens, B.: Analyzing the Arctic Feedback Mechanism between Sea Ice and Low-Level Clouds Using 34 Years of Satellite Observations, *J. Clim.*, 33, 7479 – 7501, <https://doi.org/10.1175/JCLI-D-19-0895.1>, 2020.
- Previdi, M., Smith, K. L., and Polvani, L. M.: Arctic amplification of climate change: a review of underlying mechanisms, *Environ. Res. Lett.*, 16, 093 003, <https://doi.org/10.1088/1748-9326/ac1c29>, 2021.
- 460 Rathke, C. and Fischer, J.: Retrieval of Cloud Microphysical Properties from Thermal Infrared Observations by a Fast Iterative Radiance Fitting Method, *J. Atmos. Ocean. Tech.*, 17, 1509 – 1524, [https://doi.org/10.1175/1520-0426\(2000\)017<1509:ROCMF>2.0.CO;2](https://doi.org/10.1175/1520-0426(2000)017<1509:ROCMF>2.0.CO;2), 2000.
- Rathke, C., Notholt, J., Fischer, J., and Herber, A.: Properties of coastal Antarctic aerosol from combined FTIR spectrometer and sun photometer measurements, *Geophys. Res. Lett.*, 29, 46–1, <https://doi.org/10.1029/2002GL015395>, 2002.
- Ren, L., Yang, Y., Wang, H., Zhang, R., Wang, P., and Liao, H.: Source attribution of Arctic black carbon and sulfate aerosols and associated Arctic surface warming during 1980–2018, *Atmos. Chem. Phys.*, 20, 9067–9085, <https://doi.org/10.5194/acp-20-9067-2020>, 2020.
- 465 Revercomb, H. E., Buijs, H., Howell, H. B., LaPorte, D. D., Smith, W. L., and Sromovsky, L. A.: Radiometric calibration of IR Fourier transform spectrometers: solution to a problem with the High-Resolution Interferometer Sounder, *Appl. Opt.*, 27, 3210–3218, <https://doi.org/10.1364/AO.27.003210>, 1988.
- Richter, P., Palm, M., Weinzierl, C., Griesche, H., Rowe, P. M., and Notholt, J.: A dataset of microphysical cloud parameters, retrieved from Fourier-transform infrared (FTIR) emission spectra measured in Arctic summer 2017, *Earth Syst. Sci. Data*, 14, 2767–2784, <https://doi.org/10.5194/essd-14-2767-2022>, 2022.
- 470 Ritter, C., Neuber, R., Schulz, A., Markowicz, K., Stachlewska, I., Lisok, J., Makuch, P., Pakszys, P., Markuszewski, P., Rozwadowska, A., Petelski, T., Zielinski, T., Becagli, S., Traversi, R., Udisti, R., and Gausa, M.: 2014 iAREA campaign on aerosol in Spitsbergen – Part 2: Optical properties from Raman-lidar and in-situ observations at Ny-Ålesund, *Atmospheric Environment*, 141, 1–19, <https://doi.org/https://doi.org/10.1016/j.atmosenv.2016.05.053>, 2016.
- 475 Rodgers, C. D.: *Inverse methods for atmospheric sounding: theory and practice*, vol. 2, World scientific, 2000.
- Rowe, P. M., Neshyba, S., and Walden, V. P.: Radiative consequences of low-temperature infrared refractive indices for supercooled water clouds, *Atmos. Chem. Phys.*, 13, 11 925–11 933, <https://doi.org/10.5194/acp-13-11925-2013>, 2013.
- Schmale, J., Zieger, P., and Ekman, A. M.: Aerosols in current and future Arctic climate, *Nat. Clim. Change*, 11, 95–105, <https://doi.org/10.1038/s41558-020-00969-5>, 2021.
- 480 Schmeisser, L., Backman, J., Ogren, J. A., Andrews, E., Asmi, E., Starkweather, S., Uttal, T., Fiebig, M., Sharma, S., Eleftheriadis, K., Vratolis, S., Bergin, M., Tunved, P., and Jefferson, A.: Seasonality of aerosol optical properties in the Arctic, *Atmos. Chem. Phys.*, 18, 11 599–11 622, <https://doi.org/10.5194/acp-18-11599-2018>, 2018.

- Schulz, H., Zanatta, M., Bozem, H., Leaitch, W. R., Herber, A. B., Burkart, J., Willis, M. D., Kunkel, D., Hoor, P. M., Abbatt, J. P. D., and  
485 Gerdes, R.: High Arctic aircraft measurements characterising black carbon vertical variability in spring and summer, *Atmos. Chem. Phys.*,  
19, 2361–2384, <https://doi.org/10.5194/acp-19-2361-2019>, 2019.
- Serreze, M. C. and Barry, R. G.: Processes and impacts of Arctic amplification: A research synthesis, *Global and Planetary Change*, 77,  
85–96, <https://doi.org/https://doi.org/10.1016/j.gloplacha.2011.03.004>, 2011.
- Shaw, G. E.: The Arctic Haze Phenomenon, *Bull. Am. Meteorol. Soc.*, 76, 2403 – 2414, <https://doi.org/10.1175/1520->  
490 0477(1995)076<2403:TAHP>2.0.CO;2, 1995.
- Soden, B. J. and Held, I. M.: An Assessment of Climate Feedbacks in Coupled Ocean–Atmosphere Models, *J. Clim.*, 19, 3354 – 3360,  
<https://doi.org/10.1175/JCLI3799.1>, 2006.
- Stamnes, K., Tsay, S.-C., Wiscombe, W., and Jayaweera, K.: Numerically stable algorithm for discrete-ordinate-method radiative transfer in  
multiple scattering and emitting layered media, *Appl. Opt.*, 27, 2502–2509, <https://doi.org/10.1364/AO.27.002502>, 1988.
- 495 Struthers, H., Ekman, A. M. L., Glantz, P., Iversen, T., Kirkevåg, A., Mårtensson, E. M., Seland, Ø., and Nilsson, E. D.: The ef-  
fect of sea ice loss on sea salt aerosol concentrations and the radiative balance in the Arctic, *Atmos. Chem. Phys.*, 11, 3459–3477,  
<https://doi.org/10.5194/acp-11-3459-2011>, 2011.
- Taylor, P. C., Cai, M., Hu, A., Meehl, J., Washington, W., and Zhang, G. J.: A Decomposition of Feedback Contributions to Polar Warming  
Amplification, *J. Clim.*, 26, 7023 – 7043, <https://doi.org/10.1175/JCLI-D-12-00696.1>, 2013.
- 500 Turner, D. D.: Arctic Mixed-Phase Cloud Properties from AERI Lidar Observations: Algorithm and Results from SHEBA, *J. Appl. Meteorol.*,  
44, 427 – 444, <https://doi.org/10.1175/JAM2208.1>, 2005.
- Turner, D. D.: Ground-based infrared retrievals of optical depth, effective radius, and composition of airborne mineral dust above the Sahel,  
*J. Geophys. Res.: Atmos.*, 113, <https://doi.org/https://doi.org/10.1029/2008JD010054>, 2008.
- Wagner, R., Kaufmann, J., Möhler, O., Saathoff, H., Schnaiter, M., Ullrich, R., and Leisner, T.: Heterogeneous Ice Nucle-  
505 ation Ability of NaCl and Sea Salt Aerosol Particles at Cirrus Temperatures, *J. Geophys. Res.: Atmos.*, 123, 2841–2860,  
<https://doi.org/https://doi.org/10.1002/2017JD027864>, 2018.
- Wendisch, M., Brückner, M., Burrows, J., Crewell, S., Dethloff, K., Ebell, K., Lüpkes, C., Macke, A., Notholt, J., Quaas, J., et al.: Under-  
standing causes and effects of rapid warming in the Arctic, *Eos*, 98, <https://doi.org/10.1029/2017EO064803>, 2017.
- Zanatta, M., Laj, P., Gysel, M., Baltensperger, U., Vratolis, S., Eleftheriadis, K., Kondo, Y., Dubuisson, P., Winiarek, V., Kazadzis, S., Tunved,  
510 P., and Jacobi, H.-W.: Effects of mixing state on optical and radiative properties of black carbon in the European Arctic, *Atmos. Chem.*  
*Phys.*, 18, 14 037–14 057, <https://doi.org/10.5194/acp-18-14037-2018>, 2018.

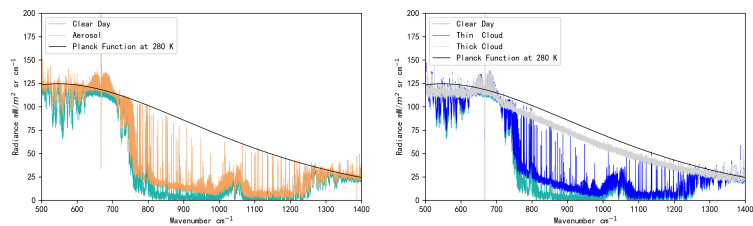


**Figure 1.** Four different emission spectra measured by NYAEM-FTS in clear sky (green), aerosol (yellow, left), thin cloud (blue, right) and thick cloud (gray, right) event respectively. The radiance calculated using Planck function at 280 K (black line) is presented in this figure. Note: the emission around  $650\text{ cm}^{-1}$  originates in ambient  $\text{CO}_2$  from the laboratory air.

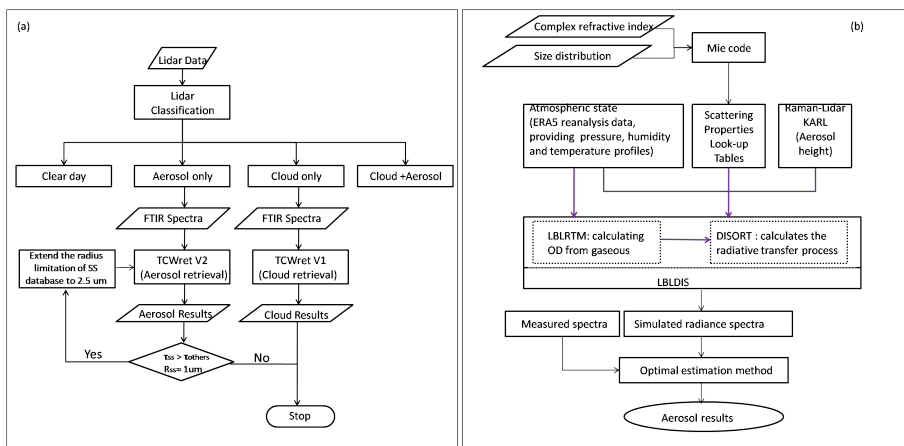


**Figure 2.** Instruments Joint Observation Scheme (a) and flow diagram of TCWRET-V2 (b).

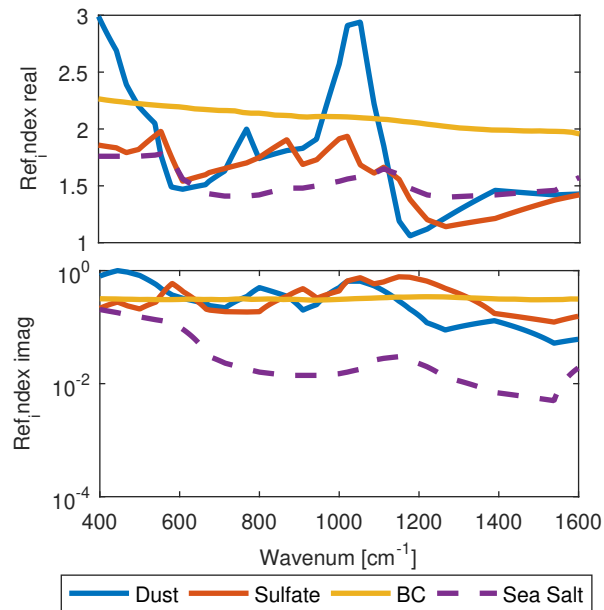


**Figure 3.** The complex refractive index of dust, sulfate, BC, and sea salt. The complex imaginary refractive index of sulfate and dust are based on OPAC/GADA database, BC from Chang and Charalampopoulos (1990), sea salt from Eldridge and Palik (1997), and Palik (1997). Those data have been downloaded from: <http://eodg.atm.ox.ac.uk/ARIA/>.

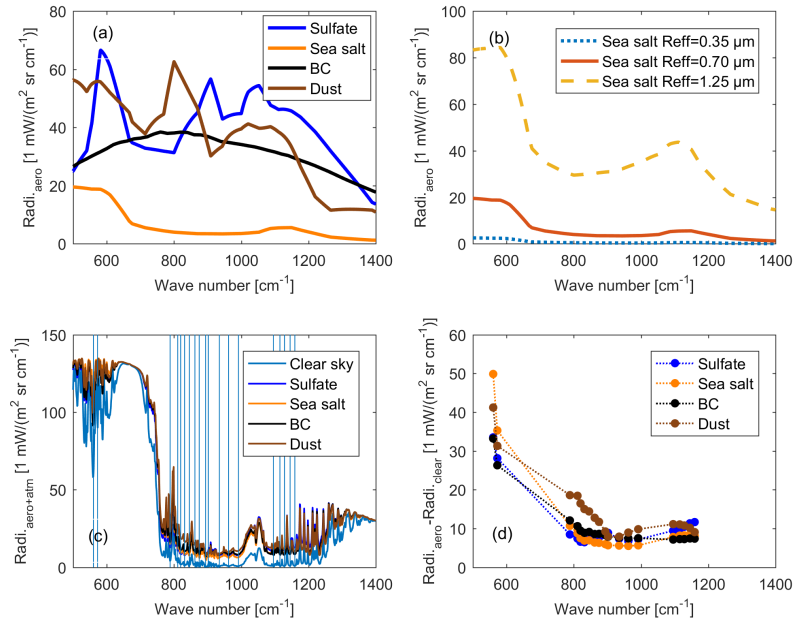


**Figure 4.** The emission spectra of small aerosol particles (dust in brown, sulfate in blue, sea salt in orange, BC in black) with  $\text{Reff} = 0.35 \mu\text{m}$  and number density =  $2000 \text{ cm}^{-3}$  (a); The emission spectra of sea salt with different particle sizes (b); The emission spectra of aerosols ( $\text{AOD}_{900 \text{ cm}^{-1}} = 0.1$ ) with atmosphere gases and clear sky case (c); The difference between total emission spectra of aerosol and clear sky case in micro windows (d). The vertical blue lines in (c) show the mid-values of micro windows selected for retrieval. The emission spectra are simulated from LBLDIS with the resolution of  $1 \text{ cm}^{-1}$ .

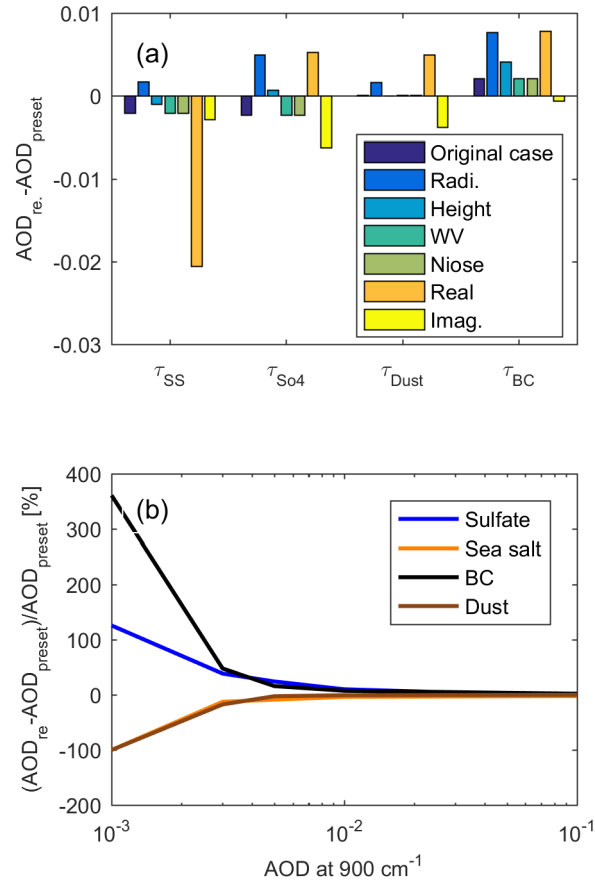


**Figure 5.** The difference between retrieved AOD in original case and several possible perturbing scenery (compare Table 2.) with preset values (a). The relative uncertainties of AOD in original cases with several preset values (b). Note: The artificial spectra with several preset values in (b) means the AOD's of aerosols are set from 0.001 to 0.1. With the same method but for different preset AODs, the reliable range of AOD are given in (b).

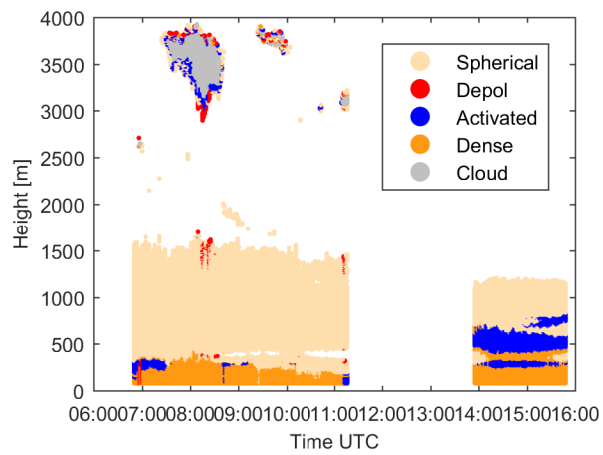


**Figure 6.** Four different aerosol classes (spherical particles in light yellow, depolarization particles in red, activated particles in blue, and dense particles in deep yellow) and cloud (gray) based on Lidar classification method on 10<sup>th</sup> of June 2020.

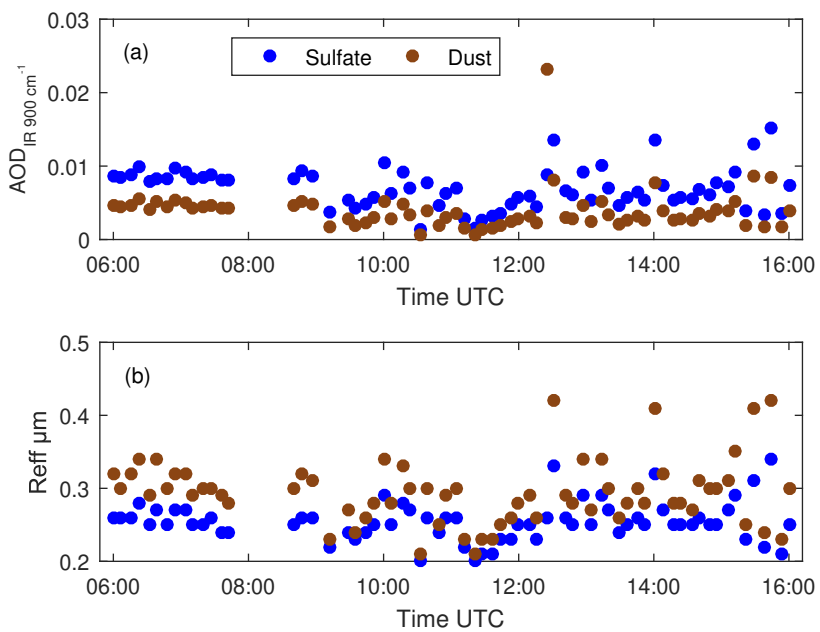


**Figure 7.** AOD of sulfate (blue) and dust (brown) retrieved from emission FTS measurements (a) and  $R_{\text{eff}}$  results with same color information (b) on 10<sup>th</sup> of June 2020.

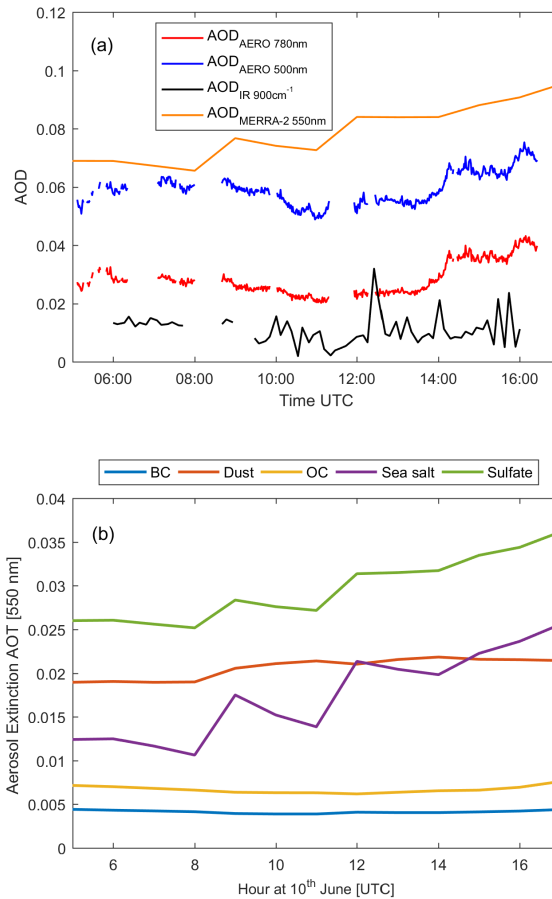


**Figure 8.** AOD measured by Sun-photometer (AERONET, 500 nm in blue and 780 nm in red), AOD measured by FTS ( $900\text{ cm}^{-1}$  in black) and AOD from MERRA-2 reanalysis data (550 nm) in Ny-Ålesund on 10<sup>th</sup> of June 2020 (a); AOD of different aerosol components in MERRA-2 reanalysis data in Ny-Ålesund on 10<sup>th</sup> of June 2020 (b). AERONET data from: <https://www.mdpi.com/2072-4292/11/11/1362>; MERRA-2 data from: <https://goldsmr4.gesdisc.eosdis.nasa.gov/data/MERRA2/M2T1NXAER.5.12.4/>.

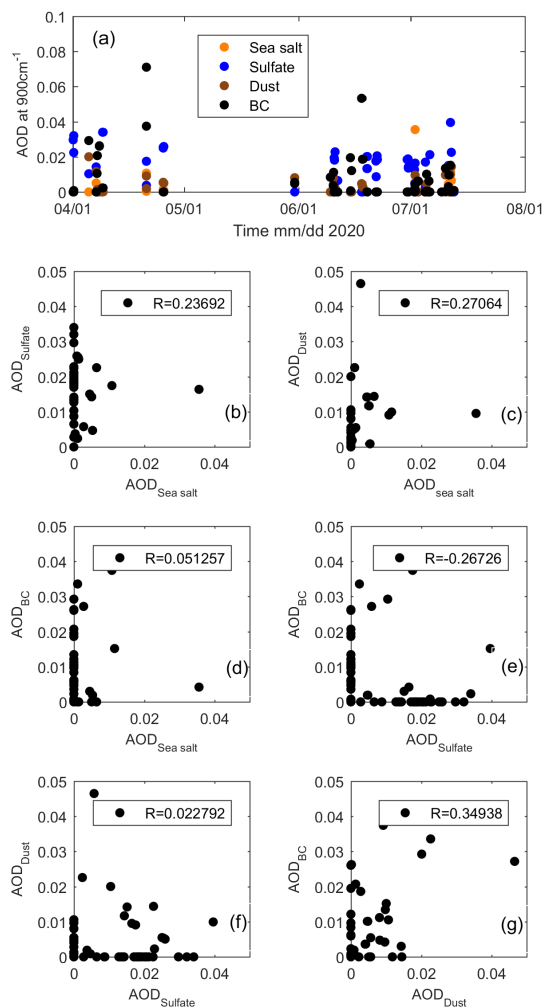


**Figure 9.** Long time period observation using FTS from April to August (a), The correlation between sea salt and sulfate (b); The correlation between sea salt and dust (c); The correlation between sea salt and BC (d); The correlation between sulfate and BC (e); The correlation between sulfate and dust (f); Th correlation between dust and BC (g).

**Table 1.** Aerosol classification by Lidar measurements as given by Ritter et al. (2016)

Classes	$\beta_{532}^{aer} (Mm^{-1}sr^{-1})$	$\delta_{532}^{aer}$	CR	Description
Clear day	$\beta < 0.4$	$\delta < 2.05\%$		Clear day
Clear depol.	$\beta < 0.4$	$\delta \geq 2.05\%$		Clear day with polarized signal.
Spherical Aerosol	$0.4 \leq \beta < 1$	$\delta < 2.05\%$		Spherical fine particles, possibly from long-distance transportation, e.g. sulfate.
Depol. Aerosol	$0.4 \leq \beta < 1$	$\delta \geq 2.05\%$		Polarized fine particles with irregular shapes, e.g. dust.
Activated Aerosol	$1 \leq \beta \leq 3$	$\delta < 2.05\%$	$CR < 1.7$	Aerosol hygroscopic growth into larger size, e.g. sea salt, sulfates.
Dense Aerosol	$1 \leq \beta \leq 3$		$CR \geq 1.7$	Medium size aerosol, e.g. sea salt, dust.
Cloud	$\beta > 3$			Cloud

**Table 2.** Parameter errors and modifications in artificial spectra

Parameters	Modifications
Height of aerosol	+10% (200 m)
Water vapor profiles	-10%
Calibration error	+1 mW/sr*m2*cm-1
Measurement error	Normally distributed noise with mean value of 0 and variance of 1
Complex refractive index (real part)	-10%
Complex refractive index (imaginary part)	-10%

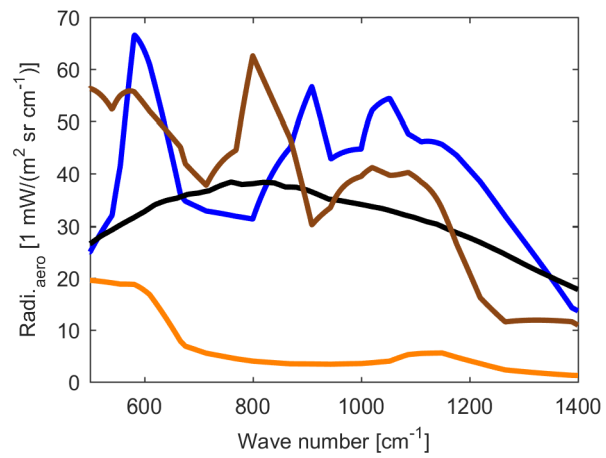


**Figure A1.** The emission spectra of large aerosol particles (dust in brown, sulfate in blue, sea salt in orange, BC in black) with  $Reff = 0.70 \mu\text{m}$  and number density =  $2000 \text{ cm}^{-3}$ .

---

Interval ( $\text{cm}^{-1}$ )
558.5–562.0
571.0–574.0
785.9–790.7
809.5–813.5
815.3–824.4
828.3–834.6
842.8–848.1
860.1–864.0
872.2–877.5
891.9–895.8
898.2–905.4
929.6–939.7
959.9–964.3
985.0–991.5
1092.2–1098.1
1113.3–1116.6
1124.4–1132.6
1142.2–1148.0
1155.2–1163.4

---

**Figure A2.** Microwindows used in TCWRET to retrieve the microphysical aerosol or cloud parameters (Richter et al., 2022).